Journal of Materials Chemistry C

PAPER

View Article Online
View Journal | View Issue

Cite this: J. Mater. Chem. C, 2017, 5, 754

Ambipolar charge distribution in donor–acceptor polymer field-effect transistors†

Xin Yu Chin,[a] Giuseppina Pace,*[b] Cesare Soci[ac] and Mario Caironi*[b]

Received 19th November 2016,
Accepted 14th December 2016

DOI: 10.1039/c6tc05033f

www.rsc.org/MaterialsC

Recent developments in the design and synthesis of donor–acceptor semiconducting copolymers have significantly contributed to improve the ambipolar transport properties of polymer field-effect transistors (FETs). The further development of such FETs towards real applications would greatly benefit from the knowledge of the specific charge distribution along the channel, especially in the ambipolar regime. Here we accomplish this task by adopting charge modulation spectroscopy (CMS) and microscopy (CMM), electro-optical spectroscopy techniques which allow us to probe *in situ* charge induced features in the transmission spectra of conjugated polymers, to study a model high mobility donor–acceptor co-polymer (DPPT-TT, poly(*N*-alkyldiketopyrrolo-pyrrole dithienylthieno[3,2-*b*]thiophene)). Thanks to the sub-micrometer spatial resolution of confocal microscopy, we are able to isolate the specific contribution of channel and electrode regions which are superimposed in the macroscopic CMS spectra, thus allowing the mapping of hole and electron distributions across the active channel in both unipolar and ambipolar operating regimes. Our findings illustrate the use of a local probe in charge-modulation experiments to correctly assign spectral features and to determine the distributions of positive and negative charge carriers in an operating device, which has relevant implications on the understanding of the nature of charge transport in high-mobility ambipolar semiconducting polymers.

1. Introduction

Conjugated polymers are semiconductors whose solubility in common organic solvents and room temperature processability allow the cost-effective manufacturing of large-area electronics on flexible substrates.[1,2] A wide range of applications have been explored with this class of materials, and much effort has been devoted to the enhancement of the transport properties of materials through improved molecular design.[3–9] Molecular design enables the control over the bandgap of polymers,[10] as well as their charge transfer and transport properties. So far, one of the most established approaches to achieve high mobility in these materials is to synthesize a π-conjugated system with alternating electron donor (D) and acceptor (A) repeating units. The extent of charge transfer and transport in these π-conjugated D–A copolymers is strongly dependent on the strengths and the nature of the intra- and inter-molecular electronic couplings.[4] This approach led to the development of high performance semiconductors employed in photovoltaic cells and high-mobility ambipolar field-effect transistors (FETs).[11,12] The ambipolar charge transport of D–A conjugated polymers can be directly assessed by measuring the electron and hole mobilities in FETs,[13] while the nature of the polaronic species in these systems can be studied with charge modulation spectroscopy (CMS).[14–16]

CMS is an electro-optical and contactless technique that allows the *in situ* measurement of charge-induced features in the transmission spectra of organic semiconductors owing to the modulation of the accumulated carriers in the channel of an operating FET.[17–19] An excess charge hosted on a conjugated molecule induces a bleaching of the ground state absorption, appearing as an increased transmission, and a specific absorption appearing at lower energies owing to polaronic relaxations.[17] Such signatures have been very useful for the description of the nature and localization/delocalization of carriers in organic semiconductors.[20–22] Importantly, in a CMS experiment, since only mobile carriers can follow the modulation, the spectral information is inherently sensitive only to conjugated segments which are actually contributing to transport in the nanometer thick accumulated channel which accumulates at the buried semiconductor/dielectric interface.[17,18,23] Another interesting feature of CMS is that by applying appropriate gating polarities

[a] Division of Physics and Applied Physics, School of Physical and Mathematical Sciences, Nanyang Technological University, 21 Nanyang Link, Singapore 637371
[b] Center for Nano Science and Technology @PoliMi, Istituto Italiano di Tecnologia, Via G. Pascoli 70/3, 20133 Milano, Italy. E-mail: giuseppina.pace@iit.it, mario.caironi@iit.it
[c] Centre for Disruptive Photonic Technologies, Nanyang Technological University, 21 Nanyang Link, Singapore 637371

† Electronic supplementary information (ESI) available: The quadrature phase of CMS and EA spectra, and carrier mapping in the hole accumulation mode. See DOI: 10.1039/c6tc05033f

to a FET capable of efficiently accumulating both hole and electrons, namely an ambipolar FET, the spectral features induced by both carriers can be probed on the same device and within the same film microstructure.[14–16] A limitation of CMS is the lack of spatial resolution, since typically the whole area of the device is probed at the same time.

We recently demonstrated the possibility of gain spatial resolution by combining CMS with an optical microscope in a confocal geometry, in the so called charge modulation microscopy (CMM) technique.[24] On the one hand, local charge modulation spectra can be acquired within the FET channel,[25] and on the other, by raster scanning the focused optical beam at a fixed energy falling within charge-induced bands, a sub-micrometer mapping of the quasi-static distribution of the mobile carriers along the accumulated FET channel, in different operating regimes, can be obtained. The use of a polarized probe further allows us to map the orientation of charged transition dipole moments and, with the support of density functional theory (DFT) calculations, to investigate at the same time the relationship between the microstructure, especially in extended non-crystalline orientated domains as obtained in uniaxially aligned films,[26] and charge transport properties.[25,27] So far, CMM has been adopted only to probe polymer FETs operating in the unipolar regime, where a single carrier type is accumulated within the FET channel.

In this work, we report the mapping of the distribution of carriers, both in unipolar and ambipolar accumulation regimes, in ambipolar FETs based on the high mobility D–A copolymer poly(*N*-alkyldiketopyrrolo-pyrrole dithienylthieno[3,2-*b*]thiophene) (DPPT-TT, Fig. 1(a)). To achieve this, we first make use of CMM by recording local spectra with high spatial resolution along the active device area to distinguish between genuine charge induced features and electroabsorption (EA) bands, allowing us to correctly assign all spectral peaks and to select a correct probe energy for the charge carrier mapping. We clearly show that CMS spectra probed over the whole device area can contain a superposition of charge-induced contributions dominating within the center of the channel, and EA contributions that become significant at the contact edges due to the field dropping on the semiconductor as a result of the injection process. Since intra- and inter-molecular polarons have overlapping features with EA peaks,[17] the spatial resolution offered by CMM greatly simplifies the assignment of

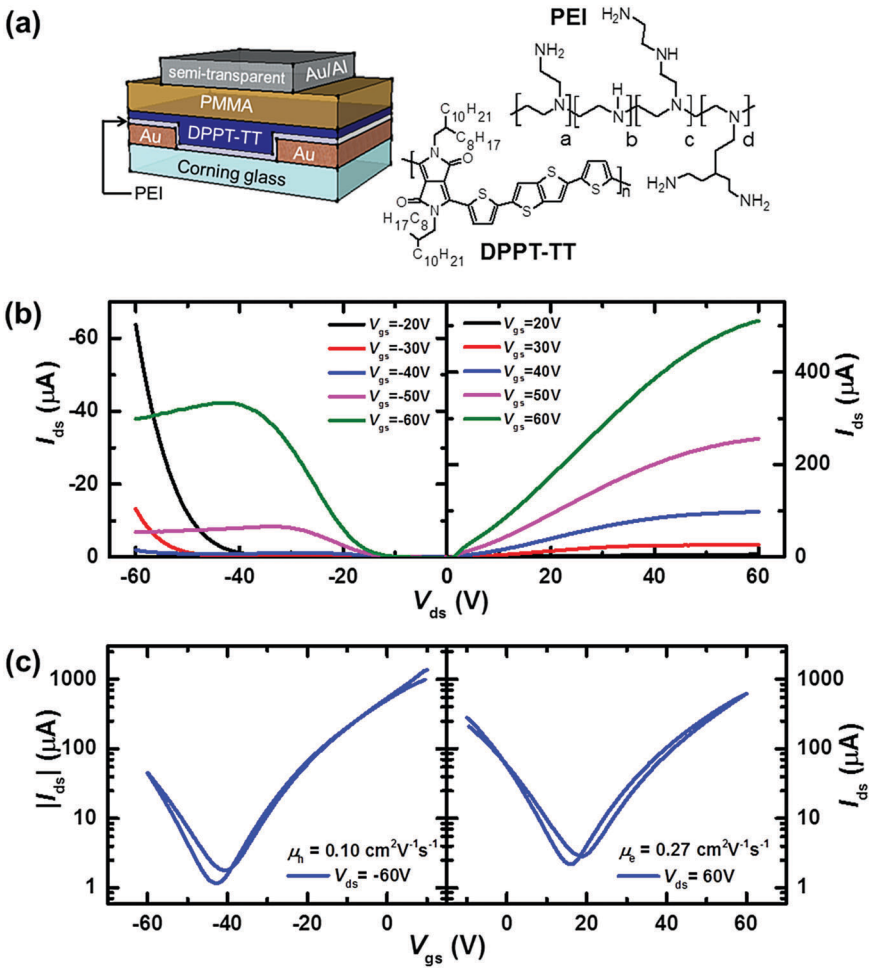

Fig. 1 DPPT-TT FET configuration and characterization. (a) FET configuration and molecular structures of the active material DPPT-TT and surface modifier PEI used in this study. Output (b) and transfer (c) characteristics of the FET device. The channel length and width are 20 μm and 20 mm, respectively.

appropriate spectral features and therefore also contributes to the study of the nature of charged species in D–A copolymers. Finally, making use of such information, we are able to safely assess the spatial distribution of holes and electrons in the DPPT-TT FET. Different from other techniques which have been used to map the potential profiles in FETs, such as the Kelvin probe[28] or second harmonic generation microscopy,[29] our detected signal correlates directly with the density of mobile charges accumulated in the operating FET, and poses no restriction on the device structure. Thus, unipolar and ambipolar regimes accessed under different biasing conditions can be clearly distinguished, providing a unique tool to gather local transport parameters of charge carriers of both species in different material systems and device configurations.

2. Experimental

2.1 Device fabrication

For FET fabrication, Corning 1737F glass was used as a substrate for top-gate bottom-contact device configuration. Interdigitated bottom electrodes with a channel width (W) of 20 mm and length (L) of 20 μm are defined with a lift-off photolithographic process. 30 nm of Au over a 0.7 nm thick Cr adhesion layer are deposited as the source and drain electrodes by thermal evaporation. A solution of branched polyethylenimine (PEI, Sigma Aldrich, M_w = 25 kg mol^{-1}) in methoxyethanol with a weight concentration of 0.4% was then spin coated onto the substrates, followed by annealing at 100 °C for 10 min on a hot plate in ambient air. The PEI surface was then washed with a mild flow of distilled water for 1 minute and dried with nitrogen flow. Reference devices without the inclusion of PEI were also fabricated. DPPT-TT (LT-S9118, Lumtec Corp., M_w > 30 kg mol^{-1}) was used as purchased. A 5 mg ml^{-1} solution of DPPT-TT in dichlorobenzene (filtered with 0.2 μm PTFE filter) was used to spincoat the active layer. The deposited DPPT-TT thin film was first thermally annealed at 160 °C for 30 minutes, and then annealed overnight at 130 °C. 500 nm of the PMMA dielectric layer (poly(methyl methacrylate), Sigma-Aldrich, M_w = 120 kg mol^{-1}) was spun from a solution in *n*-butylacetate (80 mg ml^{-1}, filtered with a 0.45 μm PTFE filter), followed by overnight thermal annealing at 130 °C. The dielectric specific capacitance is ∼5 nF cm^{-2}. A semitransparent bilayer gate made of 4 nm Au on top of 8 nm Al was then deposited by thermal evaporation. In the end, the device was thermally annealed overnight at 130 °C. Metal–insulator–semiconductor (MIS) structures were also fabricated, starting from an ITO (indium tin oxide) coated glass used as the substrate. The DPPT-TT thin film was deposited by spincoating a 5 mg ml^{-1} solution in dichlorobenzene (filtered with 0.2 μm PTFE filter). A PMMA layer (∼120 nm) was then deposited from a solution in *n*-butylacetate (20 mg ml^{-1}, filtered with a 0.45 μm PTFE filter), followed by thermal annealing for 2 hours. 80 nm of Au were deposited to complete the MIS fabrication. The entire fabrication process was completed in a nitrogen controlled environment.

2.2 Work function measurement

The work function measurement was performed in ambient conditions by means of a commercial Kelvin Probe set-up from KP technology. Au was thermally evaporated on a mica substrate, on top of a Cr adhesion layer. Measurements were performed on solvent rinsed Au, with and without PEI.

2.3 Device characterization

An Agilent B1500A semiconductor parameter analyzer was used to perform the electrical measurement of FET characteristic curves in a controlled nitrogen environment on a Wentworth Laboratories probe station. Saturation field-effect mobilities of holes and electrons were extracted from the transfer characteristic curves according to the gradual channel approximation model,[13,30] following the expression $I_d = (W/2L)\mu_{sat}C_i(V_g - V_{th})^2$, where I_d is the drain current, μ_{sat} is the saturation mobility, C_i is the dielectric capacitance per unit area, V_g is the gate voltage, and V_{th} is the threshold voltage.

2.4 Charge modulation spectroscopy (CMS) on FETs

CMS measurements were performed on FET devices with a homemade vacuum chamber with electrical feedthroughs in a high vacuum (∼10^{-5} mbar). During CMS, the source and drain electrodes are grounded. A waveform generator (Keithley 3390) and a voltage amplifier (Falco Systems WMA-300) were used to modulate the applied voltage on the gate electrode. A monochromated tungsten lamp light was used as the probing source. The light was focused on the device and the transmitted light signal was again focused and aligned on a silicon photodetector (Thorlabs FDS100). The signal was then amplified with a transimpedance amplifier (Femto DHPCA-100) and delivered to a lock-in amplifier (Stanford Instrument SR830) to obtain the differential transmission signal, ΔT. With the same lock-in amplifier technique, the transmission signal T can be acquired by modulating the monochromatic light with an optical chopper (Stanford Instrument SR540) instead of modulating the applied voltage. The $\Delta T/T$ CMS spectrum is then obtained by plotting the first harmonic ΔT (1ω) component normalized to the total T transmittance signal.

2.5 Electroabsorption (EA) on MIS

EA measurements were performed on the MIS structures within the same vacuum chamber and with the same opto-electronic setup adopted for the CMS experiment. The ITO electrode of the MIS was grounded, and the voltage on the Au electrode was modulated. The measurement was performed in reflectance configuration, with the reflected light focused on the Si detector. The differential reflectance ΔR was retrieved at first (1ω) and second (2ω) harmonics thanks to a lock-in amplifier. To obtain the normalized differential reflectance signals $\Delta R/R(1\omega)$ and $\Delta R/R(2\omega)$, the total reflectance R was acquired on the lock-in by modulating the monochromatic light.

2.6 Charge modulation microscopy (CMM)

CMM was performed on a custom-made confocal microscope, according to the setup sketched in Fig. S1 in the ESI.† Complete details have been previously reported in ref. 25. The white light generated from the supercontinuum laser (NKT Photonics SuperK Extreme) is coupled to an acousto-optic modulator

(NKT Photonics SuperK Select) to obtain monochromatic light in the 475–1100 nm region with line widths between 2 and 5 nm. A half-wave plate and a linear polarizer were used to manipulate the polarization of the monochromatic light. The incident beam on the FET device is obtained by focusing the monochromatic light with a 0.7 N.A. objective (Nikon S Plan Fluor 60×), while a 0.75 N.A. objective (Nikon CFI Plan Apochromat VC 20×) is used to collect the transmitted light from the sample. The collected light was then focused on a multimode fiber with a 50 μm diameter core, which acts as the confocal aperture. The intensity of the collected light was registered using a silicon photodetector (Thorlabs FDS100), and the collected signal was amplified by a transimpedance amplifier (Femto DHPCA-100). The amplified signal was then delivered to a DAQ (to record the transmission signal, T) and to a lock-in amplifier (Stanford Research Systems SR830 DSP) to obtain the differential transmission signal, ΔT. The CMS and EA signals are then obtained by dividing the first and second harmonic components of the differential transmission signal by the total transmission signal ($\Delta T/T$), respectively. A custom Labview program was written to perform the data collection as well as to interface the laser system and a 3D piezo stage (Physik Instrumente P-517) to perform the raster scan of the sample with a single wavelength and to collect a local spectrum at specific positions of the sample. A continuous flow of nitrogen was applied to a homemade chamber with electrical feedthroughs to keep the sample in an inert atmosphere for the entire duration of the measurement. The voltage modulation at the gate electrode is obtained by amplifying the voltage signal from the waveform generator (Keithley 3390) with a voltage amplifier (Falco Systems WMA-300). The gate modulation is fixed at frequency f = 1137 Hz unless otherwise specified. Prior to each measurement, the phase of the lock-in amplifier is synchronized to the amplified voltage modulation signal from the voltage amplifier at the first harmonic detection of the lock-in amplifier. A dual channel source-measure unit (Agilent B2912A) is used to apply the drain and source voltage.

3. Results and discussion

3.1 Field-effect transistor characterization

We first aimed at fabricating an ambipolar FET by adopting the D–A copolymer DPPT-TT, known for having high mobility and giving rise to ambipolar charge transport properties when adopted in common FET architectures[10,31–33] thanks to the properly designed D–A couple, which induces a relatively small energy band-gap, besides the closely packed stacking configuration of the polymer chains in the solid-state.[10] The device has a bottom-contact, top-gate configuration (Fig. 1(a)) and it is semitransparent to allow performing the CMS study as well as CMM mapping in the transmission mode. By adopting bare Au source and drain contacts, we obtained largely unbalanced ambipolar characteristics, with about one order of magnitude higher apparent field-effect mobility for holes (0.15 $cm^2 V^{-1} s^{-1}$) than for electrons (0.01 $cm^2 V^{-1} s^{-1}$) in the saturation regime. The corresponding FET characteristic curves are reported in the ESI† (Fig. S2). Such unbalance can be partly attributed to poor electron injection from the bare Au contacts, and did not allow us to perform comparative CMS measurements.[31,32] Therefore, in order to achieve a better balanced ambipolar behaviour and consequently FETs with comparable apparent hole and electron mobilities, we inserted an electron injection interlayer between the contacts and the semiconductor to reduce contact resistance for electrons, a commonly adopted technique to engineer charge injection in FETs.[34] As an interlayer we adopted PEI (Fig. 1(a)), a solution processable cationic polymer known to largely reduce the work-function of a large set of high work function electrodes, including Au.[35] Kelvin Probe measurements show that the work function of solvent rinsed, bare Au contacts adopted in our devices is in the range of 4.8–5.0 eV, a value that reduces to 4.2 eV when PEI is deposited on top of them (Table S1, ESI†). The ambipolar output and transfer characteristics of the resulting device are shown in Fig. 1(b) and (c). As a consequence of the PEI insertion, we obtained highly improved currents in the electron accumulation (e-accumulation) regime[23,24] (positive gate bias) and partly sacrifying FET hole accumulation (h-accumulation) regime characteristics (negative gate bias) due to the higher injection barrier seen by holes, as evident from the non-linear dependence at low drain–source voltages in the hole accumulation regime. A direct comparison of FET electrical curves with and without the PEI interlayer is reported in the ESI,† Fig. S2.[36,37] We have extracted saturation mobilities for electrons and holes from FET transfer characteristics at gate V_{gs} = 58 V and −58 V (Fig. 1(c)), corresponding to 0.27 and 0.10 $cm^2 V^{-1} s^{-1}$, respectively; threshold voltages are 30.1 V and −46.8 V, for the e- and h-accumulation mode, respectively. These mobilities are lower than those reported in previous publications (0.1–1.0 $cm^2 V^{-1} s^{-1}$ for electron mobility and 1–10 $cm^2 V^{-1} s^{-1}$ for hole mobility).[10,31,32,38] We attribute this discrepancy to the different molecular weight of the active material, known to have a strong effect especially for DPPT-TT,[39] as well as to the different device architecture[13] and fabrication processing[10] adopted in this study. Nevertheless, the fabricated FETs possess good and balanced mobilities that are suitable for investigating the charge transport properties in unipolar and ambipolar FET regimes using CMS and CMM.

3.2 Charge modulation spectroscopy and electroabsorption characterization

CMS allows us to study the charged excitations in organic semiconductors, which give rise to specific spectral fingerprints in the transmission spectrum, in the form of bleaching of the ground state absorption and in the appearance of new charge absorption features.[14,15] In this experiment the change in transmission of a probing light relative to the total transmission ($\Delta T/T$), owing to the modulation of mobile carrier density in a FET at the buried semiconductor–dielectric interface, is recorded. FETs are biased with a constant DC voltage and charge carrier modulation is achieved by superimposing an alternating component (AC) gate voltage.

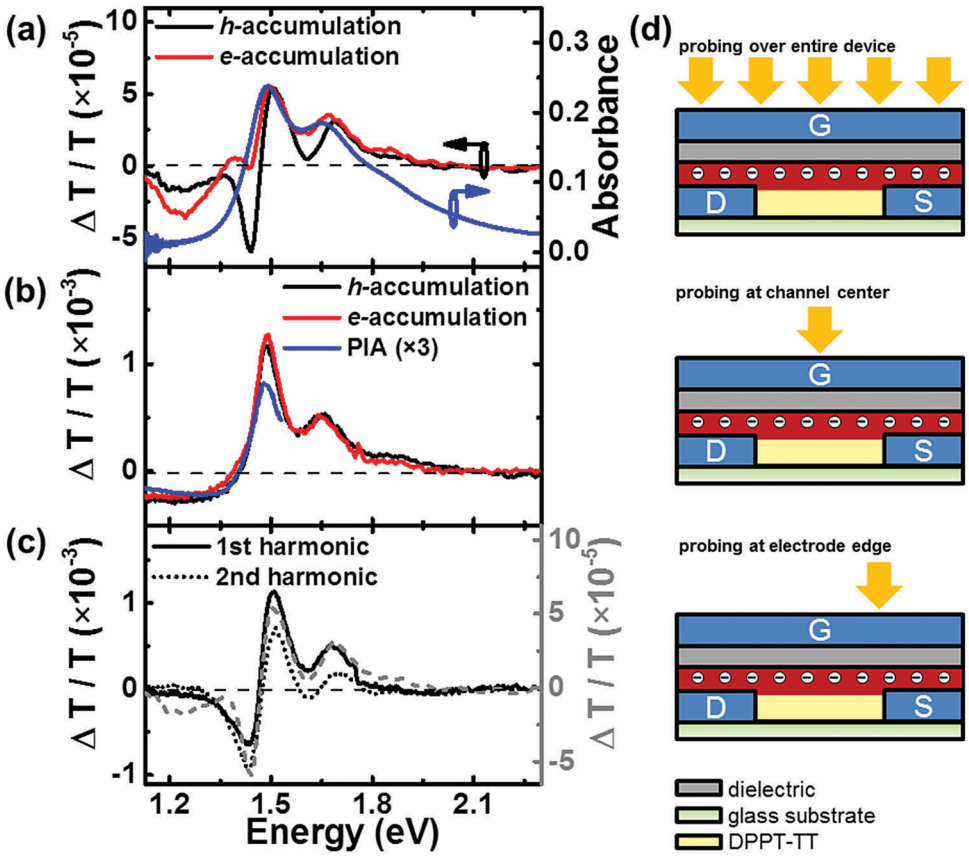

Fig. 2 (a) Macroscopic CMS spectra for hole (black, $V_{gs} = -40$ V ± 10 V) and electron (red, $V_{gs} = 40$ V ± 10 V) accumulation regimes collected by probing the entire FET device. The spectra are acquired with the source and drain electrodes at ground ($V_s = V_d = 0$ V). Absorbance of the DPPT-TT thin film is reported in blue. (b) Local CMS spectra for h-accumulation (black, $V_{gs} = -50$ V ± 10 V) and e-accumulation (red, $V_{gs} = 40$ V ± 10 V) regimes acquired by probing at the FET channel center. The blue curve shows the photo-induced absorption spectra of DPPT-TT : PCBM (1 : 4) (taken from ref. 38) (c) 1st harmonic (black continuous) and 2nd harmonic (black dotted) CMS local spectra acquired at the electrode edge. The spectra are acquired with $V_{gs} = -40$ V ± 20 V and $V_{ds} = 0$ V. The macroscopic CMS spectrum for h-accumulation (as shown in (a)) is also reported as a grey dashed line for comparison. (d) Schematics of the optical probing area (illustrated with the yellow arrow(s)) associated with the CMS spectra shown in (a), (b), and (c) (from top to bottom, respectively). Panels from a to c show the in phase signals, while the corresponding quadrature phase signals are reported in Fig. S4 (ESI†).

To investigate charge induced features in DPPT-TT, we measured $\Delta T/T$ spectra in a working DPPT-TT FET in two different gate bias regimes, *i.e.* h- and e-accumulation, which can be induced by respectively biasing the gate negative or positive with respect to the source and drain electrodes. Fig. 2(a) shows the macroscopic CMS spectra acquired under h- and e-accumulation (black and red curves, respectively) probing over the entire FET device area (spot size ~ 1 mm in diameter), with both source and drain electrodes held at ground bias ($V_s = V_d = 0$ V) and by modulating the gate voltage with the same voltage AC component around a constant gate bias of +40 V for electrons and −40 V for holes. In this configuration, the $\Delta T/T$ signal is collected both from the channel and electrode area.

The $\Delta T/T$ spectra show the bleaching of the ground-state absorption ($\Delta T/T > 0$) from roughly 1.46 eV to 2.25 eV, and charge-induced polaronic optical transitions at lower energies. The positive peaks at 1.50 eV and 1.69 eV, and the shoulder at 1.86 eV in the bleaching region resemble the DPPT-TT absorption spectrum in both accumulation regimes (Fig. 2(a), blue curve). Despite the different threshold voltages for h- and e-accumulation, the intensity of the bleaching signals is similar for both regimes: this is due to the fact that when the device is biased in full accumulation, the CMS signal depends only on the amplitude of the modulation, which determines through the device capacitance, the density of charge which is being modulated, and not on the gate bias, *i.e.* the constant accumulated charge density.

In the infrared region (from 1.46 eV to 1.13 eV), the spectra reveal instead marked differences between the h- and e-accumulation. Efforts on elucidating the origin of these different spectral features have been previously made using ambipolar FET devices.[38] Through a combination of photo-induced absorption, chemical-induced absorption, and DFT calculation, Xu *et al.* identified three different features appearing at 0.8 eV, 1.11 eV, and 1.38 eV, attributed to transitions within a monomer unit, a staggered dimer stacking, and a co-facial dimer stacking, respectively. On this basis, it was concluded that strong intermolecular coupling in the DPPT-TT fosters a two-dimensional (2D) delocalization of both holes and electrons

within at least two polymer chains.[38] In the low energy part, our h-accumulation CMS spectra display a strong and sharp negative peak at 1.44 eV, which is much weaker in e-accumulation. This peak overlaps with the absorption tail of DPPT-TT and is blue-shifted by 0.06 eV compared to the co-facial dimer stacking peak at 1.38 eV reported by Xu *et al.*[38] Another charge induced absorption band is observed between 1.13 eV and 1.37 eV for both hole and electron accumulation. The similarity of the strong absorption peak at 1.44 eV for h-accumulation with the reported absorption peak at 1.38 eV in ref. 38 suggests that this peak is likely affected by a different spectral superposition with the bleaching signal in the two cases. The presence of a much weaker feature at the same energy in the e-accumulation mode of our CMS experiment (Fig. 2(a), red curve) led us to further analyze peak assignments by acquiring local spectra along the channel.

When acquiring CMS spectra in the center of the channel (Fig. 2(b)) thanks to the use of a confocal microscope[24] (spot size $\sim$ 600 nm for 1.49 eV probing energy), both the bleaching and the charge-induced absorption features appear to be similar for h- and e-accumulation. In particular, no sharp peaks are present in the charge-induced absorption, which manifests as a single broad and flat band below $\sim$1.38 eV, down to the setup limit at 1.13 eV. This is very different from macroscopic CMS spectra in Fig. 2(a). We also acquired a local h-accumulation spectrum focusing the spot at the electrode edge (Fig. 2(c), black curve): in this spectrum we can see the presence of a sharp negative feature with a peak around 1.43 eV, very similar to what we observe in the macroscopic CMS spectrum in the h-accumulation regime (Fig. 2(a), black curve). This is the first indication that the CMS spectrum acquired over the whole device can see the superposition of different spectral contributions.

To investigate this discrepancy further, we acquired the second harmonic (2ω) of the $\Delta T/T$ signal, *i.e.* at double the gate modulation angular frequency, with the probe focused at the electrode edge. We found that the negative peak at 1.43 eV is present in the second harmonic spectrum as well (Fig. 2(c), black dotted curve). Since the modulated charge density is linearly dependent on the amplitude of the gate modulation, no charge signals can appear when acquiring at 2ω, and only field dependent EA optical transitions can contribute. We also notice that the 1.43 eV feature is similar to the second derivative of the DPPT-TT thin film absorption spectrum (Fig. S3, red curve, ESI†). This suggests that, compared to the local spectra collected at the channel center, the CMS spectrum acquired at the electrode edge contains a strong contribution from EA, which reveals also in the spectrum acquired over the entire device. To confirm the origin of the EA signal in both macroscopic and local CMS measurements at the electrodes, we performed EA spectroscopy on a DPPT-TT MIS structure (inset of Fig. S6(a), details of EA are available in the ESI†). As shown in Fig. S6(b) (ESI†), the 1ω (black curve) and 2ω (red curve) spectra of the DPPT-TT MIS show the same spectral features as the local spectrum collected at the electrode edge (Fig. 2(c), black curve). Therefore the negative peak found at around 1.42–1.43 eV, as observed both in macroscopic CMS spectra (Fig. 2(a)) and local 1ω and 2ω CMS spectra probed at the electrode edge (Fig. 2(c)), is a signature of EA. We also noticed that the zero-crossover from the bleaching characteristics to charge-induced absorption in the 2ω spectrum (Fig. 2(b), black dotted curve) collected at the electrode edge is slightly blue-shifted with respect to the 1ω spectrum (Fig. 2(c), black curve). This blue-shifted feature can be attributed to the fact that the 2ω spectrum has only EA dependence, while the 1ω spectrum allows the superposition of signals from charge absorption and EA.

The evidence of EA contribution to CMS spectra, arising from the electrode region, superimposed on the charge absorption, can be explained by a weak screening of the field induced by the gate voltage due to inefficient charge carrier injection.[17,40] The EA band is unique due to the Stark shift of the neutral polymer optical transitions owing to a strong voltage drop at the electrode. We also studied charge injection from the electrode by recording the dependence on V_{gs} of 1ω and 2ω signals at a probe photon energy of 1.49 eV corresponding to the electrode edge. The data are reported in Fig. S5 and a detailed discussion is available in the ESI.† The EA feature at 1.43 eV is also weakly present in the e-accumulation spectrum acquired over the entire device area (Fig. 2(a)). The higher EA signal contribution in the h-accumulation regime is due to a higher hole injection barrier as an effect of the use of a PEI surface modifier, which reduces the injection barrier for electrons.

The above analysis allows us to distinguish between pure charge-induced absorption, and EA effects. We would like to underline here that the genuine charge-induced CMS spectrum of DPPT-TT, that we can isolate by measuring local spectra in the middle of the channel, is very similar to photo-induced absorption (PIA, Fig. 2(b) blue curve) data reported previously for DPPT-TT.[38] The PIA spectrum shows as well a broad absorption feature below 1.40 eV, with no sharp peaks. This is consistent with our assignment of the sharp peak at 1.43 eV: such a feature cannot be present in the PIA spectrum since charge is optically generated and not injected, thus removing the possibility of having voltage drops over the polymer film originated by injection at the electrodes. Our analysis has therefore profound implications for the assignment of CMS spectroscopic features and for the understanding of the nature of charge species in D–A conjugated polymers, *e.g.* intra- *vs.* inter-chain polarons.[5,21]

3.3 Charge modulation microscopy mapping

The previous assignments allow us to safely adopt a near infrared (1100 nm, 1.13 eV) probing wavelength to map purely charge distribution, without spurious EA contributions, in the reported DPPT-TT ambipolar devices by performing CMM, a quasi-static measurement which provides information on the carrier density distribution across the FET active channel.[24,25,41] Carrier mapping of an ambipolar FET has been previously performed with a static FTIR charge modulation technique in the mid-infrared region, where the limited spatial resolution (of the order of $\sim$20 μm) of the experimental method does not allow performing the CMM studies on organic FETs with a typical channel length scale (5 to 20 μm).[16] Here we exploit the advantage of a confocal microscope and of a shorter probing wavelength to perform high resolution mapping of

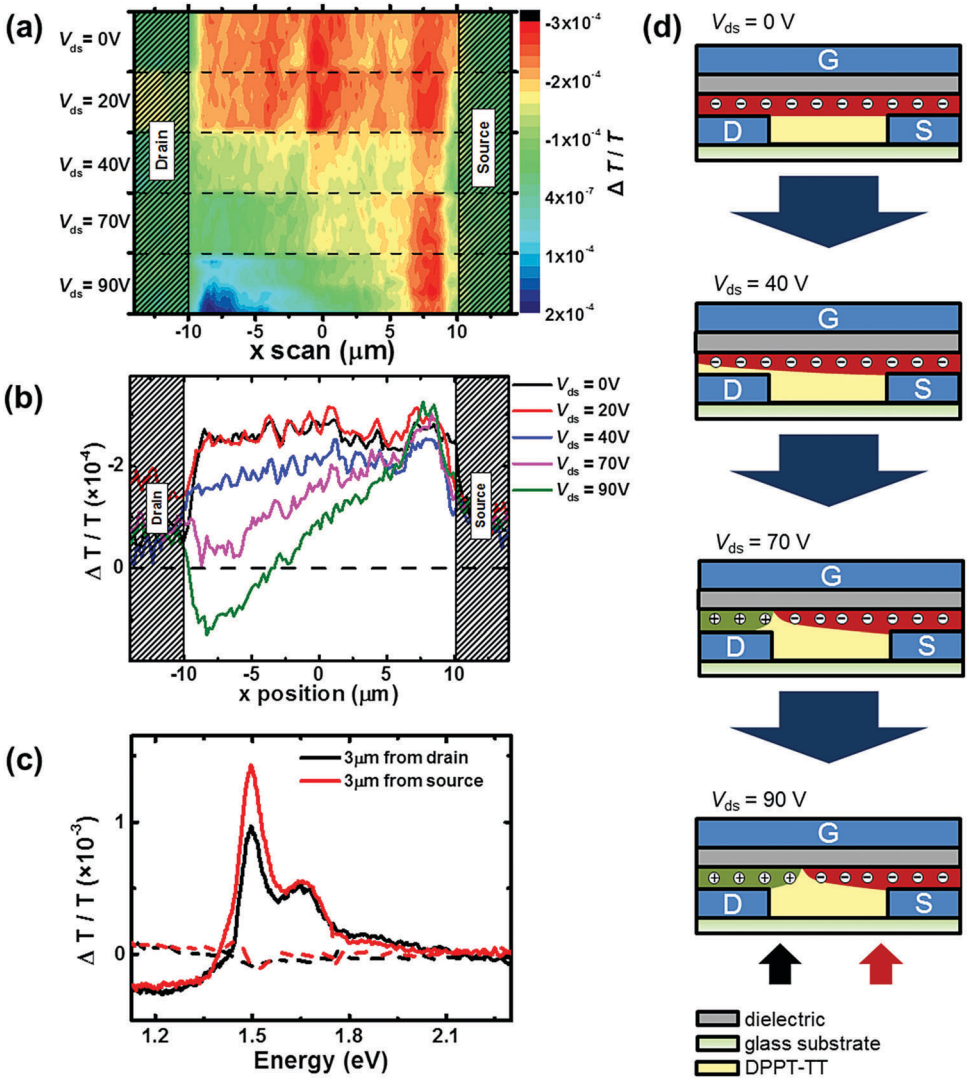

Fig. 3 (a) Charge modulation mapping of a FET operating from e-accumulation mode (V_{gs} = 30 V ± 20 V) to ambipolar accumulation, at different V_{ds} as indicated. In the *y*-direction, the height of each map at constant V_{ds} is 1.2 μm. (b) Charge modulation line profiles detected along the channel and acquired under e-accumulation (V_{gs} = 30 V ± 20 V) at different V_{ds}. The slight reduction of the electron-induced signal close to the source at the same V_{GS} bias voltage is due to device stress effects, and the difference is very close to the resolution of the technique. (c) Local spectra acquired within the active channel at ~3 μm away from drain (black) and source (red) electrode edges, with V_{gs} = 30 V ± 20 V and V_{ds} = 90 V. (d) Schematic representation of electron and hole distributions along the FET channel from e-accumulation (V_{gs} = 30 V ± 20 V) to ambipolar accumulation, at different V_{ds}. The black and red arrows indicate the position where black and red local CMS spectra shown in (c) are collected, respectively.

holes and electrons in the ambipolar FET in both unipolar and ambipolar operating regimes.

Fig. 3(a) shows the charge carrier mapping in the e-accumulation mode with different drain–source biases (V_{ds}), while the corresponding line profiles are shown in Fig. 3(b). When drain and source electrodes are grounded, the carrier density is distributed evenly across the channel. Local variations of the charge density are known to be related to the local polymer microstructure at the semiconductor–dielectric interface.[25] When increasing V_{ds}, charge density close to the drain electrode decreases with respect to the areas next to the source.[24,42] By further increasing V_{ds} from 40 V to 90 V, we first observe a vanishing charge signal next to the drain electrode, as expected from a typical FET operating in the unipolar saturation regime, and then an increasing charge signal with opposite sign. This is due to the local potential at the drain electrode exceeding the threshold voltage for opposite charge carrier injection, *i.e.* hole injection, driving the FET into an ambipolar injection regime.[13] Fig. 3(d) shows the schematic of a FET with associated profiles as shown in Fig. 3(b), which demonstrates a clean, high resolution mapping of charge carrier distribution in a polymer FET operating in the ambipolar accumulation regime. We further checked local spectroscopic fingerprints of the two carrier species concomitantly accumulated in the channel, by collecting local spectra at ~3 μm away from both source and drain electrodes (Fig. 3(c)) under ambipolar injection conditions (V_{ds} = 90 V). The collected local spectra are very similar to those local CMS spectra acquired in the channel center (Fig. 2(b)).

A similar charge carrier mapping is also performed in the h-accumulation mode (see Fig. S7, ESI†), which confirms the main observations, despite evident gate bias stress effects; a detailed discussion is available in the ESI.†

4. Conclusions

In summary, we investigated charge accumulation in an ambipolar polymer FET based on the high mobility DPPT-TT co-polymer by means of charge modulation spectroscopy and microscopy in both unipolar hole and electron accumulation modes, as well as in the ambipolar regime. We first isolated purely charge-induced spectral features due to charge modulation in DPPT-TT, which are necessary to further investigate the nature of charge carriers in such and other high mobility co-polymers. We achieved that by comparing charge-modulation spectra measured on the whole device area and local spectra where, thanks to the use of a confocal microscope, the optical probe is focused at specific points along the FET channel. We unambiguously revealed that CMS spectra collected from the whole device area contain a superposition of charge-induced absorption from the center of the channel and EA features from the electrode edge. Such EA features arise from voltage dropping over the polymer on the electrode area as a consequence of an inefficient injection process. In the case of the reported DPPT-TT device the effect is more prominent in the hole accumulation regime due to the presence of a larger barrier for hole injection. Since injection barriers are difficult to be completely eliminated, especially in ambipolar devices, we underline the relevance of the use of a local probe in order to discriminate among genuine charge-induced features and spurious EA bands. Only upon eliminating EA effects, charge-absorption spectra of both carrier species in DPPT-TT are found to be nearly identical to photo-induced spectra measured on the same polymer, where sharp transitions are not present either. We observe that it is not unusual to find sharp negative features next to the bleaching band in CMS investigations reported in the literature.[38,43] Since that is also the spectral region where charge induced absorption of inter-chain delocalized polarons should appear, care should be taken in evaluating the possible superposition of EA components which can alter the spectral shape and intensity of charge-induced features.

Thanks to the correct assignment of spectral features and the use of CMM we achieved a sub-micron resolution mapping of charge-induced absorption obtained in the EA-free near infrared spectral region, providing the first genuine visualization of charge distribution in an organic FET in the ambipolar regime. This will allow the extraction of quantitative transport parameters under linear, pinch-off, and ambipolar operating conditions for the detailed modelling of polymer transistors and their further development.

Acknowledgements

The authors are grateful to Dr Nicola Martino, Dr Alessandro Luzio, and Dr Sadir Bucella for assisting at different stages of the research. M. C. acknowledges support from the European Research Council (ERC) under the European Union's Horizon 2020 research and innovation program 'HEROIC', grant agreement 638059. This research was partly supported by the Singapore Ministry of Education (MOE2011-T3-1-005).

Notes and references

1 M. Caironi and Y.-Y. Noh, *Large area and flexible electronics*, John Wiley & Sons, 2015.
2 K.-J. Baeg, M. Caironi and Y.-Y. Noh, *Adv. Mater.*, 2013, **25**, 4210–4244.
3 C. R. Newman, C. D. Frisbie, D. A. da Silva Filho, J.-L. Brédas, P. C. Ewbank and K. R. Mann, *Chem. Mater.*, 2004, **16**, 4436–4451.
4 C. B. Nielsen, M. Turbiez and I. McCulloch, *Adv. Mater.*, 2013, **25**, 1859–1880.
5 D. Venkateshvaran, M. Nikolka, A. Sadhanala, V. Lemaur, M. Zelazny, M. Kepa, M. Hurhangee, A. J. Kronemeijer, V. Pecunia, I. Nasrallah, I. Romanov, K. Broch, I. McCulloch, D. Emin, Y. Olivier, J. Cornil, D. Beljonne and H. Sirringhaus, *Nature*, 2014, **515**, 384–388.
6 A. Marrocchi, A. Facchetti, D. Lanari, C. Petrucci and L. Vaccaro, *Energy Environ. Sci.*, 2016, **9**, 763–786.
7 S. Holliday, J. E. Donaghey and I. McCulloch, *Chem. Mater.*, 2013, **26**, 647–663.
8 B. Sun, W. Hong, Z. Yan, H. Aziz and Y. Li, *Adv. Mater.*, 2014, **26**, 2636–2642.
9 M. Sommer, *J. Mater. Chem. C*, 2014, **2**, 3088–3098.
10 J. Li, Y. Zhao, H. S. Tan, Y. Guo, C.-A. Di, G. Yu, Y. Liu, M. Lin, S. H. Lim and Y. Zhou, *Sci. Rep.*, 2012, **2**, 754.
11 X. Zhang, L. J. Richter, D. M. DeLongchamp, R. J. Kline, M. R. Hammond, I. McCulloch, M. Heeney, R. S. Ashraf, J. N. Smith and T. D. Anthopoulos, *J. Am. Chem. Soc.*, 2011, **133**, 15073–15084.
12 R. Mondal, S. Ko and Z. Bao, *J. Mater. Chem.*, 2010, **20**, 10568–10576.
13 J. Zaumseil and H. Sirringhaus, *Chem. Rev.*, 2007, **107**, 1296–1323.
14 Y. Y. Deng and H. Sirringhaus, *Phys. Rev. B: Condens. Matter Mater. Phys.*, 2005, **72**, 045207.
15 Z. Chen, M. Bird, V. Lemaur, G. Radtke, J. Cornil, M. Heeney, I. McCulloch and H. Sirringhaus, *Phys. Rev. B: Condens. Matter Mater. Phys.*, 2011, **84**, 115211.
16 O. Khatib, A. Mueller, H. Stinson, J. D. Yuen, A. Heeger and D. Basov, *Phys. Rev. B: Condens. Matter Mater. Phys.*, 2014, **90**, 235307.
17 P. J. Brown, H. Sirringhaus, M. Harrison, M. Shkunov and R. H. Friend, *Phys. Rev. B: Condens. Matter Mater. Phys.*, 2001, **63**, 125204.
18 N. Zhao, Y. Y. Noh, J. F. Chang, M. Heeney, I. McCulloch and H. Sirringhaus, *Adv. Mater.*, 2009, **21**, 3759–3763.
19 D. Fazzi and M. Caironi, *Phys. Chem. Chem. Phys.*, 2015, **17**, 8573–8590.
20 H. Sirringhaus, P. J. Brown, R. H. Friend, M. M. Nielsen, K. Bechgaard, B. M. W. Langeveld-Voss, A. J. H. Spiering,

R. A. J. Janssen, E. W. Meijer, P. Herwig and D. M. de Leeuw, *Nature*, 1999, **401**, 685–688.
21 V. D'Innocenzo, A. Luzio, A. Petrozza, D. Fazzi and M. Caironi, *Adv. Funct. Mater.*, 2014, **24**, 5584–5593.
22 A. Y. B. Meneau, Y. Olivier, T. Backlund, M. James, D. W. Breiby, J. W. Andreasen and H. Sirringhaus, *Adv. Funct. Mater.*, 2016, **26**, 2326–2333.
23 F. Maddalena, C. de Falco, M. Caironi and D. Natali, *Org. Electron.*, 2015, **17**, 304–318.
24 C. Sciascia, N. Martino, T. Schuettfort, B. Watts, G. Grancini, M. R. Antognazza, M. Zavelani-Rossi, C. R. McNeill and M. Caironi, *Adv. Mater.*, 2011, **23**, 5086–5090.
25 N. Martino, D. Fazzi, C. Sciascia, A. Luzio, M. R. Antognazza and M. Caironi, *ACS Nano*, 2014, **8**, 5968–5978.
26 S. G. Bucella, A. Luzio, E. Gann, L. Thomsen, C. R. McNeill, G. Pace, A. Perinot, Z. Chen, A. Facchetti and M. Caironi, *Nat. Commun.*, 2015, **6**, 8394.
27 N.-K. Kim, S.-Y. Jang, G. Pace, M. Caironi, W.-T. Park, D. Khim, J. Kim, D.-Y. Kim and Y.-Y. Noh, *Chem. Mater.*, 2015, **27**, 8345–8353.
28 K. P. Puntambekar, P. V. Pesavento and C. D. Frisbie, *Appl. Phys. Lett.*, 2003, **83**, 5539–5541.
29 D. Yamada, T. Manaka, E. Lim, R. Tamura and M. Iwamoto, *J. Appl. Phys.*, 2008, **103**, 084118.
30 S. M. Sze and K. K. Ng, *Physics of semiconductor devices*, John Wiley & Sons, 2006.
31 Z. Chen, M. J. Lee, R. Shahid Ashraf, Y. Gu, S. Albert-Seifried, M. Meedom Nielsen, B. Schroeder, T. D. Anthopoulos, M. Heeney and I. McCulloch, *Adv. Mater.*, 2012, **24**, 647–652.
32 Y. Li, S. P. Singh and P. Sonar, *Adv. Mater.*, 2010, **22**, 4862–4866.
33 S. Mandal, G. Dell'Erba, A. Luzio, S. G. Bucella, A. Perinot, A. Calloni, G. Berti, G. Bussetti, L. Duò, A. Facchetti, Y.-Y. Noh and M. Caironi, *Org. Electron.*, 2015, **20**, 132–141.
34 K.-J. Baeg, J. Kim, D. Khim, M. Caironi, D.-Y. Kim, I.-K. You, J. R. Quinn, A. Facchetti and Y.-Y. Noh, *ACS Appl. Mater. Interfaces*, 2011, **3**, 3205–3214.
35 Y. H. Zhou, C. Fuentes-Hernandez, J. Shim, J. Meyer, A. J. Giordano, H. Li, P. Winget, T. Papadopoulos, H. Cheun, J. Kim, M. Fenoll, A. Dindar, W. Haske, E. Najafabadi, T. M. Khan, H. Sojoudi, S. Barlow, S. Graham, J. L. Bredas, S. R. Marder, A. Kahn and B. Kippelen, *Science*, 2012, **336**, 327–332.
36 B. Sun, W. Hong, H. Aziz and Y. Li, *Polym. Chem.*, 2015, **6**, 938–945.
37 B. Sun, W. Hong, E. Thibau, H. Aziz, Z.-H. Lu and Y. Li, *Org. Electron.*, 2014, **15**, 3787–3794.
38 H. Xu, Y. Jiang, J. Li, B. S. Ong, Z. Shuai, J. Xu and N. Zhao, *J. Phys. Chem. C*, 2013, **117**, 6835–6841.
39 R. J. Kline, M. D. McGehee, E. N. Kadnikova, J. Liu, J. M. Fréchet and M. F. Toney, *Macromolecules*, 2005, **38**, 3312–3319.
40 A. Horvath, G. Weiser, G. Baker and S. Etemad, *Phys. Rev. B: Condens. Matter Mater. Phys.*, 1995, **51**, 2751.
41 C. Sciascia, M. Celebrano, M. Binda, D. Natali, G. Lanzani and J. R. Cabanillas-Gonzalez, *Org. Electron.*, 2012, **13**, 66–70.
42 X. Y. Chin, J. Yin, Z. Wang, M. Caironi and C. Soci, *Sci. Rep.*, 2014, **4**, 3626.
43 M. J. Lee, Z. Chen, R. d. Pietro, M. Heeney and H. Sirringhaus, *Chem. Mater.*, 2013, **25**, 2075–2082.